The role of holes in improving the performance of nitrogen-doped holey graphene as an active electrode material for supercapacitor and oxygen reduction reaction

CrossMark

Zhong-jie Jiang [a,*], Zhongqing Jiang [b,*], Weiheng Chen [b]

[a] New Energy Research Institute, College of Environment and Energy, South China University of Technology, Guangzhou 510006, Guangdong, China
[b] Department of Chemical Engineering, Ningbo University of Technology, Ningbo 315016, Zhejiang, China

HIGHLIGHTS

- A simple KOH etching and ball milling method is been used to synthesize NHG.
- NHG exhibits high electrochemical performance for supercapacitors.
- NHG exhibits high electrochemical performance for oxygen reduction reaction.
- The holes facilitate the formation of the NHG solid with a porous structure.
- The holes play an important role in improving the electrochemical performance of NHG.

GRAPHICAL ABSTRACT
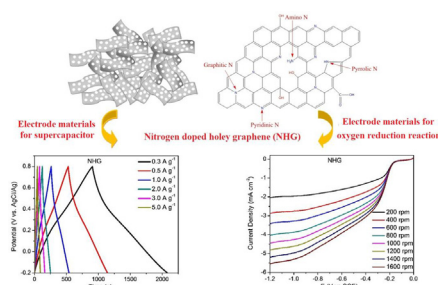
ABSTRACT

Nitrogen doped holey graphene (NHG), with in-plane holes in its sheet plate, has been synthesized in this work through the potassium hydroxide (KOH) etching and ball milling of nitrogen doped graphene (NG). It shows that the KOH etching and ball milling does not distinctly alter the elemental composition and the relative percentages of functional groups in NG, but produce holes in its in-plane sheet plate. The obtained NHG can then be used as an active electrode material for supercapacitors and as an active electrocatalyst for oxygen reduction reaction, and exhibits significantly higher electrochemical performance than the corresponding NG. Its improved electrochemical performance could be attributed to its specific holey structure in the sheet plate and porous structure in its randomly stacked solid, which provide it with more active edge atoms, better accessibility to electrolyte, larger accommodation space for ions, faster electrolyte diffusion and movement and so on.

© 2013 Elsevier B.V. All rights reserved.

1. Introduction

The ever-increasing demand for powering portable devices has triggered a burst of research towards the development of miniaturizable alternative energy sources, such as lithium ion batteries, supercapacitors, fuel cells and etc [1–6]. The practical uses of these energy sources are required to have both high energy and power densities, which depend mainly upon the chemical and physical

* Corresponding authors. Tel.: +86 020 39381202.
E-mail addresses: zhongjiejiang1978@hotmail.com, eszjiang@scut.edu.cn (Z.-j. Jiang), zhongqingjiang@hotmail.com (Z. Jiang).

properties of the electrode materials used [7–11]. Significant efforts have therefore been devoted to exploiting new materials or improving the properties of the traditional electrode materials to boost both the energy and power densities of these energy source devices [8,12–17]. From the perspective of applications, it is generally desirable to exploit active materials that can be employed as the constituents of electrodes for uses in all the types of the energy source devices. However, the development of such materials is considerably difficult since the requirements that are proposed to improve the performance of the energy source devices of different types are not same. For instance, materials for lithium ion batteries are required to have high rate capacity of Li^+ intercalation/deintercalation [1,5,18], while materials for fuel cells are required to have high electrocatalytic activities towards oxygen reduction or fuel oxidation reactions [19–22].

Recently, a new material, which is generally referred to as graphene, has attracted tremendous attentions [23–25]. Because of its excellent electrical conductivity, high surface area, good flexibility, and good chemical and environmental stability, graphene has widely been used as an electrode material for LIBs, supercapacitors, fuel cells and etc., and shows great promises to improve the performance of these energy source devices [2,10,15,26]. However, due to its unique structure which consists of a single planar sheet of sp^2-bonded carbon atoms densely packed in a honeycomb crystal lattice, the pristine graphene is prone to aggregation to form a stack with a flake-like structure due to the π–π and strong van der Waals intersheet interactions [27,28]. As a result, the diffusion of electrolytes predominantly takes place at the edge of the stack, while its diffusion across the graphene plane and into its interlayers is limited, when it is used as the electrode materials [5,29,30]. In this case, graphene might not be well utilized and the performance of the corresponding energy source devices is not well improved [27,31,32]. Great efforts have therefore been paid to the development of porous 3-dimensional graphene solids through fabricating sandwich type structures by introduction of "spacer" phases, such as, carbon nanotubes, nanoparticles and etc., or through forming 3-dimensional macroporous structures and networks by the template-directed deposition or controlled assembly of graphene [14,16,33–36]. The porous structure can promote the electrolyte solutions in/out of the electrode materials, facilitating faster electrolyte diffusion and a better utilization of active materials [14,34–37]. And additionally, the presence of holes can produce more edge atoms that are active for applications in the energy source devices [38–40]. Studies have demonstrated that the energy source devices with the electrodes containing graphene solids with a 3-dimensional porous structure usually exhibit significantly higher electrochemical performance [14,37,41–43]. An alternative way to construct the 3-dimensional porous graphene structure is to introduce in-plane holes into the graphitic nanosheets of graphene. Since the presence of the in-plane holes can increase the flexibility of the graphitic nanosheets and simultaneously decrease its van der Waals intersheet interactions, the randomly stacking of the holey graphene could lead to the formation of solids with a 3-dimensional porous structure [5,29].

Another strategy that is frequently used to improve the performance of graphene as the electrochemical materials for the energy source devices is the doping of heteroatoms into its graphitic structure [8,16,44–46]. Due to the difference in the properties between carbon and heteroatoms, the incorporation of heteroatoms can endow graphene with new properties and thus increases the usability of the graphene based materials as the electrode materials for applications in various energy source devices [36,46–50]. For example, the incorporation of N or/and B atoms into the lattice gives graphene with greatly improved electrocatalytic activity toward oxygen reduction reactions (ORR) [3,45,51]. Additionally, the presence of nitrogen on the carbon framework can also improve the

wettability of graphene toward the electrolyte solutions, thus enhancing the mass transfer efficiency, and simultaneously provide pseudocapacitance, thus increasing the energy density of supercapacitors [52,53].

The introduction of in-plane holes into the graphitic nanosheets of nitrogen-doped graphene would produce nitrogen-doped holey graphene (NHG). We would expect that NHG can be used as a promising electrode material for the energy source devices, since its holey structure can facilitate the formation of the solid with a 3-dimensional porous structure, while the doped nitrogen could improve its performance as the promising electrode material. To demonstrate this, we synthesize NHG through a procedure involving the fabrication of NG and the subsequent KOH etching and ball milling. The obtained NHG is then used as the electrode material for the supercapacitors and as the electrocatalyst for the ORR. The experimental results show that NHG can greatly improve the performance of the supercapacitors and exhibits the significantly enhanced electrocatalytic activity. The improvements in the performance of the supercapacitors and the enhancement in its electrocatalytic activity could be attributed to its holey structure and porous morphology in its randomly stacked solid, since the presence of in-plane holes in the graphene sheet plate can produce more edge atoms that are active for the charge storage and the ORR, while the presence of pores in its randomly stacked solid facilitates the fast diffusion and movement of electrolytes, allowing for the better utilization of active materials.

2. Experimental

2.1. Chemicals and reagents

TIMREX® PG25 natural graphite is obtained from TIMCAL Ltd. Concentrated sulfuric acid (H_2SO_4, 95%), methanol (CH_3OH, ≥99.7%), potassium permanganate ($KMnO_4$, ≥99.0%), sodium nitrate ($NaNO_3$, ≥99.0%), hydrochloric acid (HCl, 37%), hydrogen peroxide aqueous solution (H_2O_2, 35%), melamine (99%), and isopropanol ($CH_3CH(OH)CH_3$, ≥99.5%) are purchased from Sigma–Aldrich. The commercially available Johnson Matthey (JM) Pt/C 40 wt.% (Pt loading: 40 wt.% Pt on the carbon black) is purchased from the Johnson Matthey Corp. These chemicals are used as received without further purification. Deionized water (DI H_2O) through Millipore system (Milli-Q®) is used in all experiments.

2.2. Materials preparation

2.2.1. Preparation of GO

The synthesis of GO is done using a procedure developed by Hummers et al. [54]. Typically, 2 g of graphite and 2.5 g of $NaNO_3$ are first mixed with 150 mL of H_2SO_4 (95%) in a 500 mL flask. The mixture is then stirred for 30 min with an ice bath, which is followed by the addition of 15 g of $KMnO_4$ under vigorous stirring. The rate of the $KMnO_4$ addition is well controlled to maintain the reaction temperature below 20 °C. The reaction mixture is then stirred overnight at room temperature, followed by addition of 180 mL of H_2O also under vigorous stirring. After that, the reaction temperature is rapidly increased to 98 °C and keeps for 24 h, which leads to a color change from black to yellow. Followed by the addition of 80 mL of 35% H_2O_2 aqueous solution, the reaction mixture is cooled down to room temperature. The obtained graphene oxide is washed by rinsing and centrifugation with 5% HCl and H_2O for several times, and then filtrated and dried under vacuum.

2.2.2. Preparation of nitrogen-doped graphene (NG)

For the synthesis of NG, 40 mg of GO is first dispersed in 40 mL of H_2O by sonication. 0.2 g of melamine is then added. The obtained

mixture is stirred at 500 rpm until significant agglomeration is observed. The dark brown agglomeration is transferred to a Teflon lined autoclave for the hydrothermal reaction at 180 °C for 12 h. After it is cooled to room temperature, the obtained solution is filtrated and dried at 80 °C in an oven. The solid material is collected and homogenized into fine powders using a mortar and pestle. The composite powder is pyrolyzed at 800 °C for 1 h in a nitrogen atmosphere to obtain NG.

2.2.3. Preparation of nitrogen-doped holey graphene (NHG)

For the fabrication of NHG, 0.02 g of NG synthesized above is mixed with 80 mL of 6 M KOH, and the obtained suspension is stirred and etched for 12 h, and then milled continuously at a rotation speed of 300 rpm for 30 h on a planetary mill with zirconia balls (2.0–2.5 mm in diameter, 200 g weight) and poly(tetrafluoroethylene) vials. The resulting dark dispersion was washed with 1 mol L^{-1} HCl solution and deionized water until the filtrate becomes neutral, giving a black suspension with holey nitrogen-doped graphene sheets stably suspended in water, which is then subjected to centrifugation at 15,000 rpm for 30 min. The sample is finally dried overnight at 60 °C in an oven to obtain NHG. The yield of NHG can get up to 95%. Thus, the process used to make this material is readily scalable to industrial levels.

2.3. Sample characterizations

An environmental scanning electron microscope (Model Quanta 650 FEG) at an operation voltage of 20.0 kV is used to measure the morphology of the obtained NG and NHG solids. TEM measurements are conducted on a JEM-2100F high-resolution transmission electron microscope with an accelerating voltage of 200 kV. The chemical composition of the samples is determined by X-ray photoelectron spectroscopy (XPS) on a VG ESCALAB 250 spectrometer (Thermo Electron, U.K.), using an Al Kα X-ray source (1486 eV). Raman spectra are collected with a Renishaw inVia Raman spectrometer using an excitation wavelength of 514.5 nm (2.41 eV) from an argon ion laser. The laser power on the sample is kept below 1 mW to avoid possible laser-induced heating and the exposure time is ~5 s. A laser beam size of ~1 μm with ×100 objective lens is used. The specific surface areas of the samples are analyzed by a surface area analyzer (NOVA 2000, Quantachrome) using physical adsorption/desorption of N_2 at the liquid-N_2 temperature. Specific surface area is calculated according to the Brunauer–Emmett–Teller (BET) method.

The capacitive performance of NG and NHG is carried out in a typical three-electrode cell with 2 M H_2SO_4, while the ORR performance is performed in a N_2-saturated or O_2-saturated 0.1 M KOH aqueous solution at room temperature (25 °C). For the electrode preparation, the predetermined amounts of the corresponding graphene samples are well dispersed in isopropanol and H_2O (volume ratio, 3:2) mixture in the presence of 5 wt.% Nafion under sonication to prepare 5 mg ml^{-1} and 1 mg ml^{-1} ink solutions for the supercapacitors and the ORR, respectively. 10 μL of the as-prepared ink is then dropped on a glassy carbon (GC) disk electrode, followed by dropping 5 μL of Nafion solution in isopropyl alcohol (0.5 wt.%) as a binder for the preparation of a smooth film for cyclic voltammograms (CV), electrochemical impedance spectra (EIS), rotating-disk electrode voltammograms and chronoamperometry measurements. For comparison, the commercial Johnson Matthey (JM) Pt/C 40 wt.% (Johnson Matthey Corp., Pt loading: 40 wt.% Pt on the carbon) electrode is also prepared. The Pt/C suspension is prepared by dispersing 10 mg of Pt/C powder in 10 mL of ethanol in the presence of 50 μL of 5 wt.% Nafion solution in isopropanol. The addition of a small amount of Nafion could effectively improve the dispersion of the Pt/C catalyst suspension. The saturated calomel electrode (SCE) and platinum mesh are served as the reference electrode and counter electrode, respectively, for the ORR electrochemical characterization. A Pt wire is used as the counter electrode and a KCl saturated Ag/AgCl electrode as the reference electrode for supercapacitors. In the chronoamperometric experiments, the stability of the catalysts against methanol is performed by addition of 3 M methanol into the O_2-saturated 0.1 M KOH aqueous solution at 380 s and the stability of the catalysts against CO is performed by introduction of 10% (v/v)
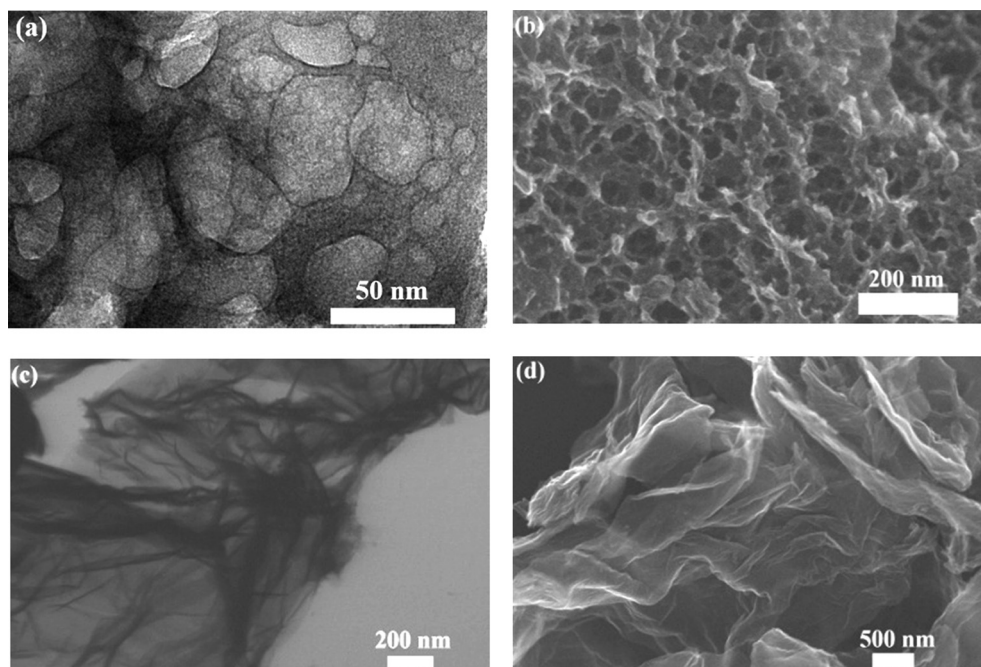

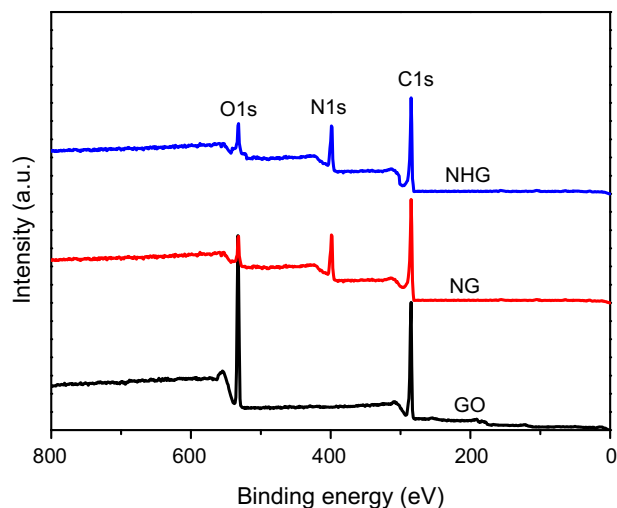**Fig. 1.** TEM and SEM images of NHG (a, b) and NG (c, d).

Fig. 2. XPS survey spectra of GO, NG, and NHG.

Fig. 3. High-resolution XPS spectra of (a) N 1s, and (b) C 1s for GO, NG, and NHG.

CO in air into the O_2-saturated 0.1 M KOH aqueous solution at 270 s. The galvanostatic charge/discharge curves for these three electrode materials are performed by Arbin BT-G-5V-10A (USA) in the three electrodes system. The electrochemical measurements of NG and NHG are tested on the conventional three-electrode system (Autolab PGSTAT302N Eco Chemie B.V and CHI 760C, USA). Electrochemical impedance spectra (EIS) are recorded under the following conditions: frequency range $0.1–10^5$ Hz, AC voltage amplitude 5 mV, and open circuit potential.

3. Results and discussion

3.1. Spectroscopic and structural characterization of NHG

Fig. 1a shows a typical TEM image of the obtained NHG synthesized following a procedure which involves the synthesis of GO, the preparation of NG via the hydrothermal reaction of GO and melamine, and the etching and ball milling of NG in the presence of KOH. Similar to its parent GO, NHG synthesized here also has a sheet-like structure, but with holes observable in its sheet plate. The KOH etching at high temperatures has indeed been widely used to produce holes in the graphene, carbon nanotubes and carbon fibers [55,56]. In the present work, we use the ball milling to promote the formation of holes in the NHG nanosheets. The ball milling cannot only facilitate the exfoliation of the graphitic nanosheets, but also facilitate the creation of the local high temperatures for the activation of carbon with KOH and the mechanochemical crack of graphitic C–C bonds [55,57–59], which promote the formation of the holes in the NHG nanosheets. The random stacking of NHG would lead to the formation of a solid with a 3-dimensional porous structure, as shown in Fig. 1b. This is unlike NG whose stacking leads to the formation of a flake-like structure due to the strong π–π and van der Waals intersheet interactions as shown in Fig. 1c and d. The formation of the 3-dimensional porous

structure in the NHG stack could be attributed to its specific holey structure and the thus induced reduction in the π–π and van der Waals interactions between the graphitic sheets.

The XPS survey spectrum shows the existence of C, N and O in NHG, as demonstrated in Fig. 2. This is different with the XPS survey spectrum of its parent GO, where only elemental C and O are identified (as shown in Fig. 2), indicating that the elemental N has been successfully incorporated into NHG through the method
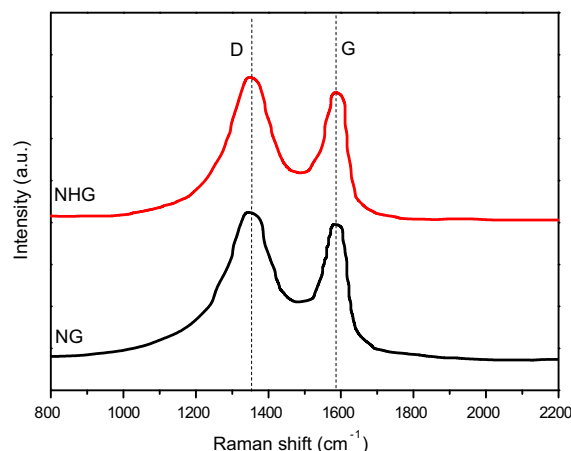
Table 1
XPS elemental analysis of GO, NG, and NHG samples.

Samples	C1s [atom%]	N1s [atom%]	O1s [atom%]
GO	40.52	0	59.48
NG	57.63	25.33	17.04
NHG	53.96	26.08	19.96

Fig. 4. Raman spectra of NG and NHG.

Table 2
N 1s and C1s XPS elemental analysis of NG and NHG samples.

Samples	N 1s [atom%]				C 1s [atom%]				
	Pyridinic N	Pyrrolic N	Graphitic N	Amino N	sp^2 C	C–OH	C–O/C=N	C–N/C=O	–O–C=O
NG	57.34	12.20	11.57	16.00	50.78	22.16	17.00	4.52	5.54
NHG	55.50	10.99	12.65	19.91	48.45	25.18	15.70	5.90	4.77

described in the experimental section. The greatly reduced intensity of the O 1s peak in NHG (as shown in Fig. 2) suggests that the oxygen containing components, which is initially dominant in the GO, have been substituted by the nitrogen containing groups or decomposed during the thermal annealing process of GO and melamine. Worth noting is that although the KOH activation and ball milling step has been employed to produce holes in NG, the results in Fig. 2 and Table 1 show that the obtained NHG has a similar elemental composition and a comparable relative elemental contents with NG, indicating that the KOH activation does not change the composition and the relative elemental contents of NG, but only produces holes in its sheet plate. To gain further insights into the structure of NHG, the deconvolution of the N 1s and C 1s spectra is done. The deconvolution spectra of N 1s in Fig. 3a show that there exist five different N components in both NG and NHG, corresponding to the pyridinic (398.3 eV), amino (399.2 eV),

pyrrolic (400.1 eV), graphitic (401.4 eV) and quaternary N (403.7 eV), respectively. These different N components could be the thermally pyrolyzing products of GO and melamine. Due to the complexity of the thermal pyrolysis, the elemental N is incorporated into graphene in the different forms. The existence of N in the multiple forms in both NG and NHG can also be demonstrated by the deconvolution spectra of C 1s shown in Fig. 3b, where the C atoms with binding energies at 286.1 and 287.3 eV can clearly be identified, indicating the existence of C=N and C–N molecular segments. In addition, the presence of the trace amounts of C–O, C=O and HO–C=O in both NG and NHG could also be identified by the devolution spectra shown in Fig. 3b, indicating that GO might not completely be reduced during the thermal annealing step in the presence of melamine, which is similar to NG reported by the other groups [38,60]. The dominance of the graphitic C as demonstrated in Fig. 3b indicates that the obtained NHG still possess a graphitic
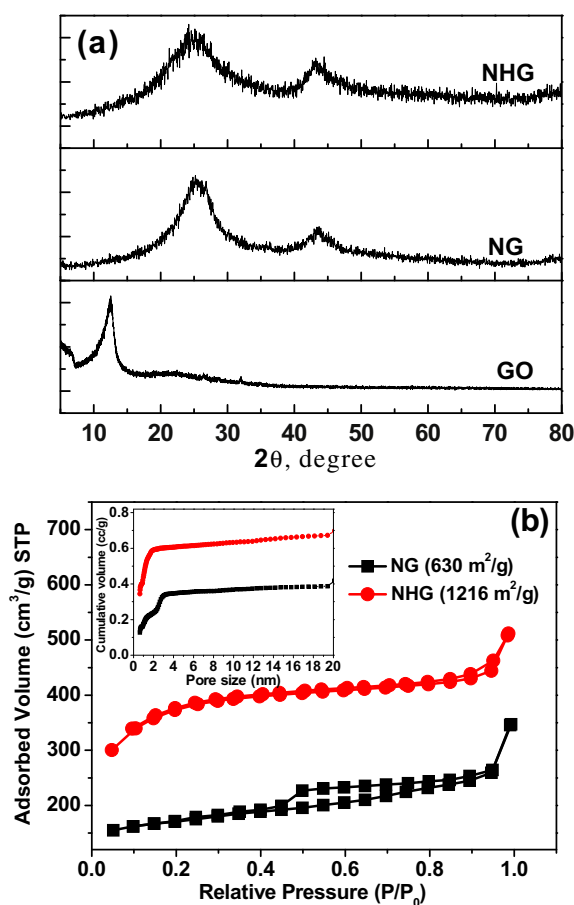

Fig. 5. (a) XRD patterns of GO, NG, and NHG. (b) Nitrogen adsorption–desorption isotherms of NG and NHG. The specific surface areas of the samples were calculated using the Brunauer–Emmett–Teller (BET) method with the adsorption data at the relative pressure (P/P$_0$) range of 0.05–0.20. The inset shows the cumulative pore volumes of NG and NHG calculated using a slit/cylindrical NLDFT model.
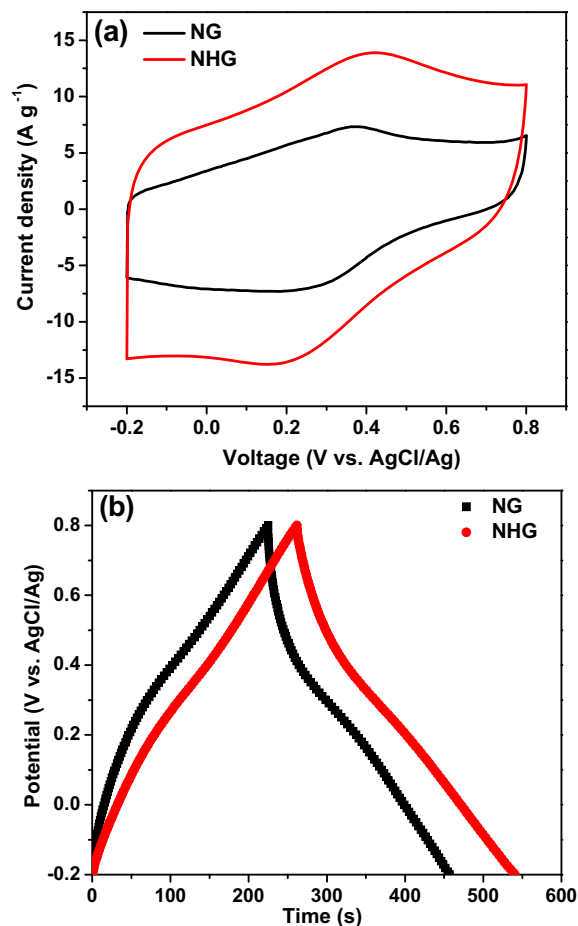

Fig. 6. (a) CV curves of NG and NHG in a three electrode system in 2 M H$_2$SO$_4$ solution at the scan rate of 50 mV s^{-1}, (b) galvanostatic charge/discharge curves of NG and NHG in the three electrode system at current density of 1 A g^{-1}. In all the cases, the same mass loadings of the electrode materials are used for the electrochemical measurements.

structure, which is also supported by the Raman spectra of NG and NHG shown in Fig. 4, where two prominent peaks corresponding to the characteristic G (the in-plane bond-stretching motion of pairs of C sp^2 atoms [61]) and D (arising from the disordered sp^2 hybridization carbon [62]) bands of the graphitic structure can be clearly seen. In good agreement with the results shown above is that the relative percentages of the various N components keeps relatively comparable after the KOH activation step, which further demonstrates that the KOH activation does not change the composition and the relative elemental contents of NG, but produces holes in its sheet plate. The slightly increased contents of the graphitic and quaternary type N in NHG, as shown in Table 2, could be attributed to the fact that the nucleophilic attack of OH$^-$ could lead to the cleavage of some double bonds of C=N, which would undoubtedly result in the slight increase in the relative contents of the graphitic and quaternary type N in NHG.

To better clarify the microstructure of the randomly stacked NHG solid, the XRD pattern of the sample is measured. Fig. 5a shows a comparison of the XRD patterns of GO, NG, and NHG. As shown in Fig. 5a, the XRD pattern of GO exhibits a peak at $2\theta = 12.5°$, which could be assigned to the (001) reflection of the GO solid corresponding to an average interlayer spacing of 0.71 nm [63]. Its decreased diffraction angle compared to that of the natural graphite reported in literature (the diffraction peak of the natural graphite appears at $2\theta = 26.6°$ [63]) could be attributed to the presence of the oxygenous groups, [54,64] such as –OH, HO–C=O, C=O and etc., which increase the interlayer spacing of the graphitic nanosheets. The thermal annealing of GO in the presence of melamine greatly reduces the oxygenous groups as demonstrated above. The XRD pattern of the obtained NG therefore exhibits a peak centered at $2\theta = 25.6°$, corresponding to an average interlayer spacing of 0.35 nm. The broader peak width compared to that of

GO, as shown in Fig. 5a, indicates the presence of pores in the randomly stacked NG solid, which can also be demonstrated by the N$_2$ adsorption–desorption isotherm shown in Fig. 5b. The KOH activation of NG does not change the XRD peak position of the obtained NG solid, albeit it exhibits a broader diffraction peak. This diffraction peak broadening could be attributed to the presence of holes in the NHG sheet plate and pores in its corresponding randomly stacked solid, as demonstrated above. The N$_2$ adsorption–desorption isotherms in Fig. 5b show that NHG has a specific surface area of 1216 m^2 g^{-1} which is significantly higher than that of NG (630 m^2 g^{-1}). This is in good agreement with the result shown in the inset of Fig. 5b that NHG exhibits a much higher cumulative pore volume than NG.

3.2. Application of NHG as the electrode material in the supercapacitor

To experimentally demonstrate that NHG can be used as an active electrode material for supercapacitors, its CV curve in a three electrode system in 2 M H$_2$SO$_4$ solution is measured, as shown in Fig. 6a. The CV curve of NHG exhibits a rectangular-like shape with one pair of broad Faradaic peaks appearing at 0.16 and 0.42 V, indicating the co-existence of electric double-layer capacitance (EDLC) and pseudocapacitance [52,65], in which the EDLC makes the main contribution on the specific capacitance of this electrode material. The co-existed pseudocapacitance could be attributed to Faradic reactions induced by lone electron pairs from the nitrogen groups interacting with the cations in the electrolyte solution [52,66]. Although the CV curve of NG performed under the same condition also exhibits a shape similar to that of NHG, its current density and curve area are indeed much lower than that of NHG in the measured potential range, as shown in Fig. 6a, which clearly
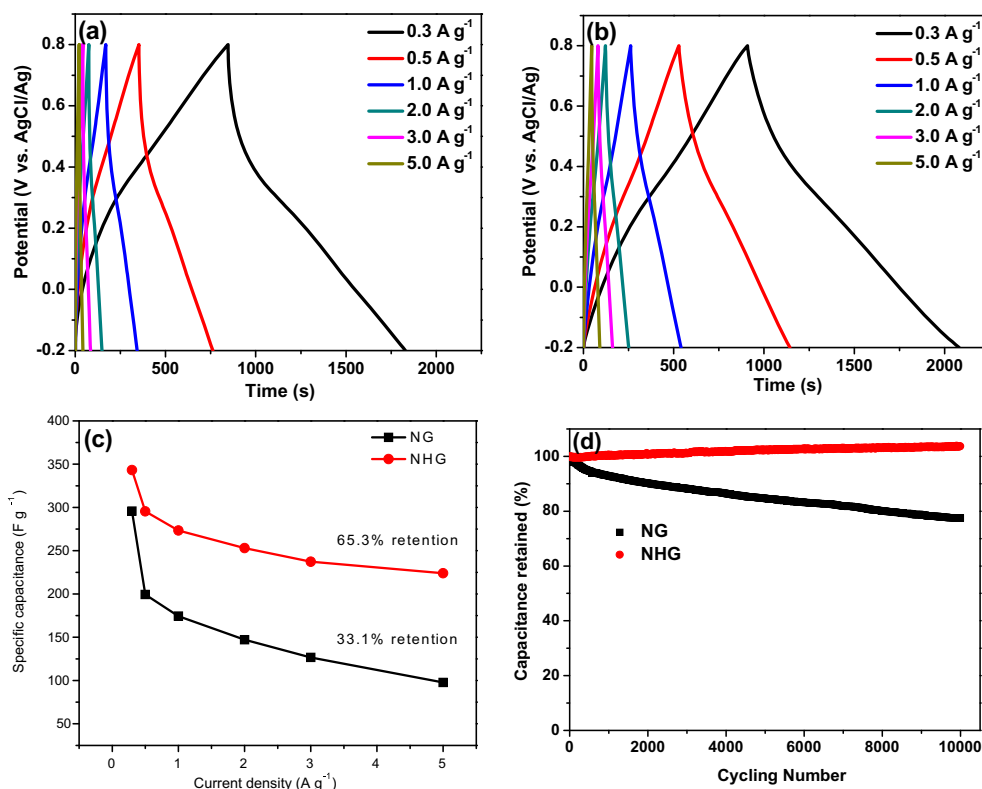

Fig. 7. Galvanostatic charge–discharge curves for (a) NG and (b) NHG at different current densities at room temperature. (c) Comparison of the specific capacitances of NG and NHG under various current densities calculated based upon the results of Fig. 7a and b. (d) Long-term cycling stability of NG and NHG performed at current density of 5 A g^{-1}.

indicates the superiority of NHG over NG as the electrode material for supercapacitors.

The electrochemical performance of NG and NHG is then further investigated with the galvanostatic charge/discharge experiments, as shown in Fig. 6b. Consistent with the results shown by the CV curves, the galvanostatic curves of NG and NHG both exhibit a non-linear charging/discharging behavior, indicating the presence of pseudocapacitive reactions due to the redox reactions occurring during the charge/discharge processes. The better performance of NHG, in comparison to NG, can be demonstrated from its longer charge and discharge times, as shown in Fig. 6b. To further demonstrate that NHG is a superior electrode material than NG, the galvanostatic charge/discharge for both NG and NHG in the three electrode system at various current densities is performed, as shown in Fig. 7a and b. Fig. 7c shows NHG has the specific capacitances (calculated based upon the galvanostatic charge/discharge curves shown in Fig. 7a and b) that are always higher than that of NG over the current densities covered in this study and exhibits much better capacitance retention performance. As shown in Fig. 7c, the specific capacitance of NHG at the current densities of 0.3, 0.5, 1.0, 2.0, 3.0 and 5 A g^{-1} is 343, 295, 273, 253, 237 and 224 F g^{-1}, respectively, while NG only gives the specific capacitance of 296, 199, 175, 147, 127 and 98 F g^{-1}, respectively, at these current densities. At the high rate of 5 A g^{-1}, NHG can maintain 65.3% retention of its initial specific capacitance measured at 0.3 A g^{-1}, while NG can only maintain 33.1% retention of its initial specific capacitance. These results clearly demonstrate the superiority of NHG over NG as the active material for supercapacitors. This is also supported by its better cycling stability compared to that of NG, as shown in Fig. 7d, indicating that the randomly stacked solid is able to retain its structural integrity during the charge/discharge processes.

The electrochemical performance of NG as the electrode material for supercapacitors has indeed been investigated previously, and it has been reported to have significantly higher rate capacity and better stability compared to the pristine graphene and other carbon related materials [36,49,50]. The higher specific capacitance

and better retention property of NHG reported in this work therefore indicate that NHG could be used as a more attractive electrode material for supercapacitors. Considering that NG and NHG have a similar elemental composition and consist of functional groups with the relatively same percentages, we will conclude here that the improved electrochemical performance of NHG originates from its holey structure and thus facilitated formation of porous structure in its randomly stacked solid. This could be plausibly reasonable since the presence of in-plane holes in the sheet plate allows the cross-plane diffusion of the electrolytes and can produce more edge atoms that are active for the charge storage, while the presence of pores in its randomly stacked solid allows the fast diffusion and movement of electrolytes and can provide more space for the charge accommodation, which improves the utilization of active materials.

For better understanding of the superior performance of NHG, its EIS spectrum is measured. Fig. 8 shows the typical Nyquist plots for both NG and NHG in the three electrode system in 2 M H$_2$SO$_4$ solution. Two major characteristic features can be observed in the high and low frequency regions corresponding to the different resistance phenomena during the electrochemical process. The semicircles at the high frequency region could be attributed to the resistance at the solid−electrolyte interface due to the discontinuity in the charge transfer process at the solid/electrolyte interface
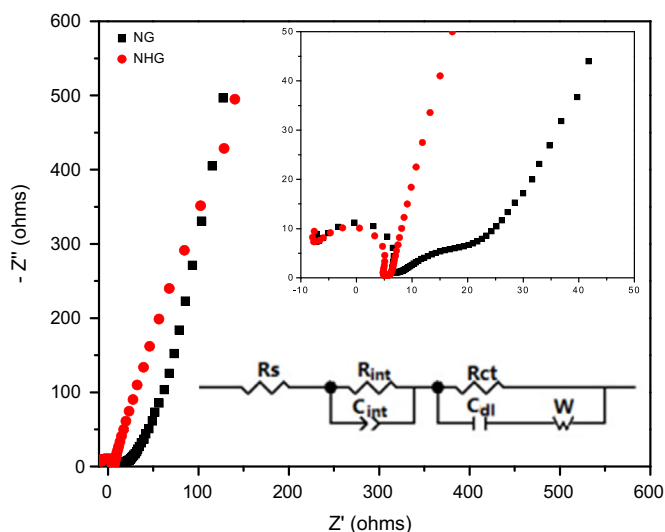

Fig. 8. Nyquist plots for NG and NHG in the three electrode system in 2 M H$_2$SO$_4$ solution. The inset shows the magnification of Nyquist plots at the high frequency region. The modified Randles equivalent circuit used to fit the data points of the EIS spectra is also given in the figure. In the circuit, R_s represents the electrolyte resistance, R_{int} and C_{int} are the resistance and capacitance at the electrode-electrolyte interface, respectively; R_{ct} and C_{dl} are the charge transfer resistance and double-layer capacitance, respectively; and W is the Warburg diffusion impedance.
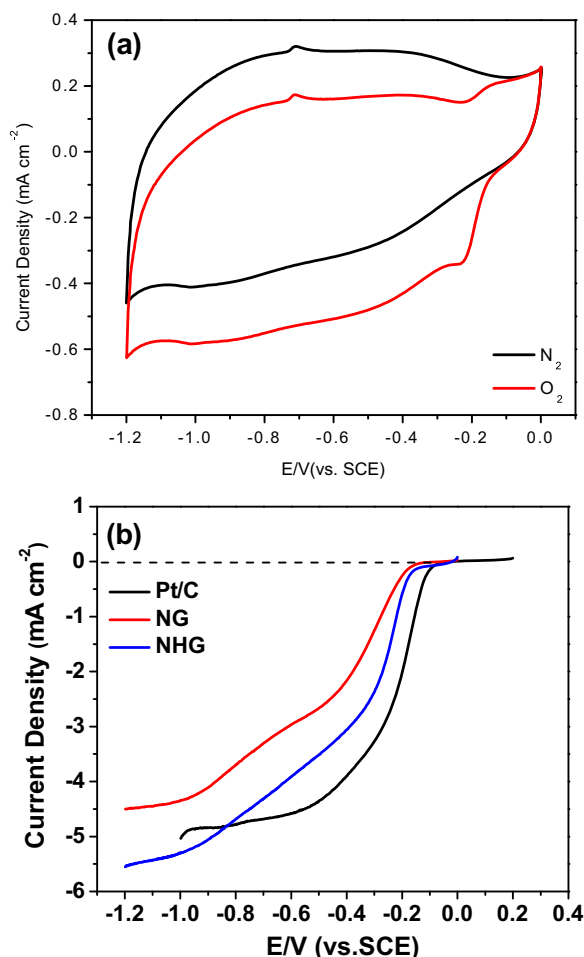

Fig. 9. (a) CV curves of NHG in O$_2$ or N$_2$ saturated 0.1 M KOH aqueous solution at a scan rate of 10 mV s^{-1}. (b) LSV curves for the oxygen reduction for the NG, NHG, and JM Pt/C electrodes in an O$_2$-saturated 0.1 M KOH solution at a scan rate of 10 mV s^{-1} and a rotation rate of 1600 rpm. The mass loadings of catalysts are ∼0.01 mg.

caused by the difference in the conductivity between the solid and the aqueous electrolyte phase. The impedance behavior in this region also involves the resistance arising from the Faradaic redox processes, as demonstrated above. The straight line at the low frequency region could be assigned to the diffusive resistance of the electrolyte with the electrode material. Based on the equivalent circuit shown in the inset of Fig. 8, it is extracted that the charge transfer resistance (R_{ct}) of NHG (4.8 Ω) is lower than that of NG (6.5 Ω), indicating the easier accessibility of the electrolyte to the surface of NHG. This might be attributed to the increased contact area of NHG to electrolytes due to its significantly higher specific surface area, as demonstrated in Fig. 5b. The faster electrolyte diffusion behavior of NHG can be demonstrated the more vertical straight line in its EIS spectra at low frequency region, indicating that the porous structures in its randomly stacked solid can facilitate the inward/outward diffusion of electrolyte ions.

3.3. Application of NHG as the active electrocatalyst for the ORR

The electrocatalytic activity of NHG toward ORR can be demonstrated by comparison of its CV curves in 0.1 M KOH aqueous solutions saturated with nitrogen or oxygen. As shown in Fig. 9a, the CV curve of NHG obtained from the N_2-satrurated solution shows a featureless voltammetric current, while its corresponding CV curve obtained from the O_2 saturated solutions exhibits a well

defined cathodic peaks at −0.22 V corresponding to the reduction of oxygen, which clearly indicates its electrocatalytic activity towards ORR. Indeed, NHG can even exhibit a higher electrocatalytic activity than NG, which can be demonstrated from its linear sweep voltammetric (LSV) curve in Fig. 9b showing a higher current density and more positive half-wave potential (i.e. the potential at which the current is half of the limiting current) compared to those of NG. Although NHG still shows lower electrocatalytic activity towards ORR than the commercial JM Pt/C 40 wt.%, as demonstrated by its more negative onset potential and lower current density at the low negative potential region, it can exhibit a higher current density at the highly negative potential region (Fig. 9b), which presumably suggests that NHG is more kinetically facile toward ORR than the JM Pt/C 40 wt.%. The better performance could be attributed to the specific structure of NHG which comprises holes in its sheet plate and pores in its randomly stacked solid, creating more edge atoms and facilitating the cross-plane diffusion of the electrolytes and a better utilization of active materials, as mentioned above.

To well understand the underlying physics associated with its high electrocatalytic activity, the LSV curves of NHG in the O_2-saturated 0.1 M KOH solutions under the various electrode rotating rates are measured. For comparison, the LSV curves of NG in the O_2-saturated 0.1 M KOH solutions under the various electrode rotating rates are also performed. The measured current intensity
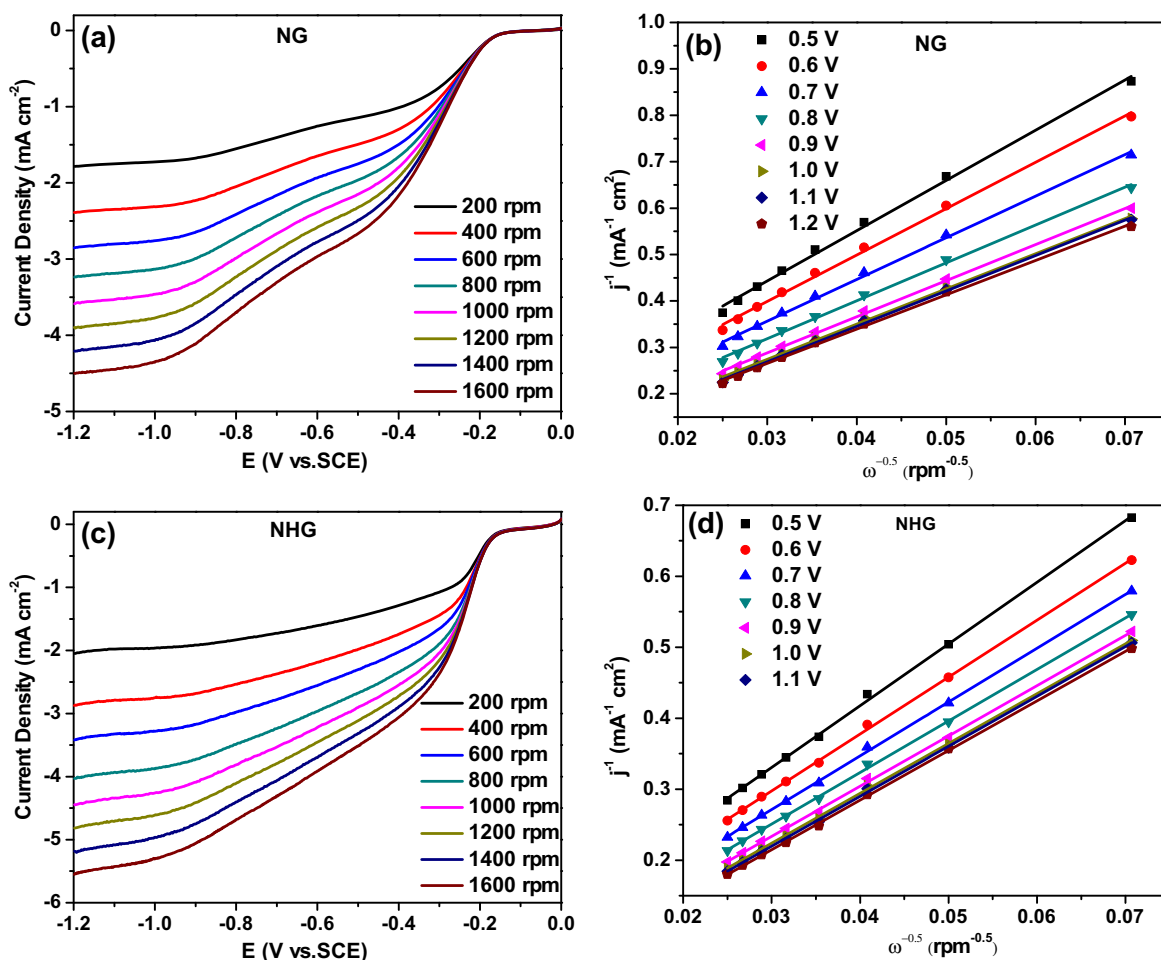

Fig. 10. (a, c) LSV curves at various different rotation rates for the oxygen reduction on the NG and NHG electrodes in an O_2-saturated 0.1 M KOH solution; (b, d) K–L plots of the NG and NHG electrodes obtained based on the data extracted from Fig. 10a and c, respectively. The dots are the experimental results and the straight lines are their corresponding fittings using Equation (1).

shows an increase with increase of the rotating rate due to the enhanced diffusion of the electrolytes, as shown in Fig. 10a and c. The ORR performance in the diffusion and kinetically limited regions is then analyzed using the Koutecky–Levich (K–L) equation [42,67]:

$$\frac{1}{J} = \frac{1}{J_L} + \frac{1}{J_K} = \frac{1}{B\omega^{1/2}} + \frac{1}{J_K} \qquad (1)$$

where J is the measured current density, J_L and J_K are the diffusion-limiting and kinetic current densities, ω is the electrode rotating rate, and B is the Levich constant. Fig. 10b and d shows the K–L plots of NG and NHG at various electrode potentials. A clear linear relationship between J^{-1} and $\omega^{-0.5}$ can be observed at a range of potentials, indicating that the ORR catalyzed by NHG is of first order with respect to the concentration of the dissolved O_2. The linear fitting of the K–L plots yields the Levich constant, which can then utilized to obtain the number of electron transferred (n) in each ORR according to the following equation [17,68]:

$$n = 0.62 \, FD^{2/3}v^{-1/6}B^{-1}C_O \qquad (2)$$

where F is Faradic constant ($F = 96486$ C mol^{-1}), D is the diffusion coefficient of O_2 in the electrolyte solution ($D = 1.9 \times 10^{-5}$ cm^2 s^{-1}), v is kinematic viscosity of the electrolyte (0.01 cm^2 s^{-1}), and C_O is the concentration of oxygen (1.2×10^{-6} mol cm^{-3}).

The occurrence of oxygen reduction in fuel cells is either via the 4-electron reduction pathway in which oxygen is directly reduced to H_2O or via the 2-electron reduction pathway involving the formation of hydrogen peroxide (H_2O_2) as an intermediate [3,69]. Generally, the 4-electron pathway is preferred, since it provides a faster oxygen reduction rate. Fig. 11a summarizes the electron transfer numbers involved in the each ORR, yielded based upon Equation (2). The electron transfer number of the ORR on NG varies from 2.6 to 3.8 at the potential range from −0.5 to −1.2 V (as shown in Fig. 11a), indicating the existence of the two-electron reduction pathway. This is in good agreement with the electron transfer number for the ORR occurring on the electrode of NG reported previously [39,60]. The electron transfer number for the ORR on the NHG electrode is always higher than that on the NG electrode over the potential range covered in this study. As shown in Fig. 11a, the electron transfer number for the ORR on the electrode of NHG ranges from 3.2 to 4.0, suggesting that the ORR on this electrode is dominated with the 4-electron pathway. This indicates that NHG is a more efficient ORR electrocatalyst than NG, which can be also demonstrated by its relatively higher kinetic current density, j_k, for the ORR with respect to the NG electrode, as shown in Fig. 11b.

To further demonstrate the superiority of NHG as the electrocatalyst for the ORR over NG, its long-term stability and tolerance to crossover and poison effects are measured. The chronoamperometric curves in Fig. 12 show that NHG exhibits a significantly higher stability than NG and the commercial Pt/C 40 wt.%. As shown in Fig. 12a, only 14.7% of the original activity of NHG has been lost over 10 h of the ORR, while the introduction of methanol and CO has no effects on the ORR activity of NHG. The high stability of NHG could be attributed to its specific molecular structure and the porous morphology of its randomly stacked solid, which are immune to the poisoning of methanol and CO and can buffer the local structure change during the electrochemical ORR process. This is unlike the commercial Pt/C 40 wt.% in which the loss of 30% its original activity has been observed over 10 h of the ORR due to the dissociation of the Pt nanoparticles from the carbon substrate or the aggregation of the Pt nanoparticles during the electrochemical processes, [70,71] while upon the introduction of methanol and CO, even more reduction of its original activity has been detected due to the block of active sites on the Pt nanoparticles by the adsorption of CO or the methanol oxidation products, [72,73] as shown in Fig. 12b and c. Although the introduction of methanol and CO has no effects on the ORR activity of NG (Fig. 12b and c), its long-term stability is indeed much lower than that of NHG. As shown in Fig. 12a, a much higher loss in the ORR activity of NG (>26%) has been observed over the 10 h of the ORR. These results indicate that NHG is a more stable ORR catalyst than the commercial Pt/C 40 wt.% and NG and can be immune to the methanol crossover and CO poison effects.

4. Conclusions

In summary, NHG, with in-plane holes in its sheet plate, has been synthesized through a procedure involving the fabrication of NG and the subsequent KOH etching and ball milling. The KOH etching and ball milling does not change the elemental composition and the relative percentages of functional groups of NG, but produce in-plane holes in its sheet plate. The electrochemical results show that NHG is an active electrode material for supercapacitors and an active electrocatalyst for the ORR, and exhibits significantly higher electrochemical performance than its unholey counterparts (i.e. NG), including higher charge/discharge capacity, more efficient toward ORR, and better long-term stability and etc. Its improved electrochemical performance could be attributed to its specific holey structure in the sheet plate and porous structure in its randomly stacked solid, which provide it with more active edge atoms, better accessibility to electrolyte, larger accommodation
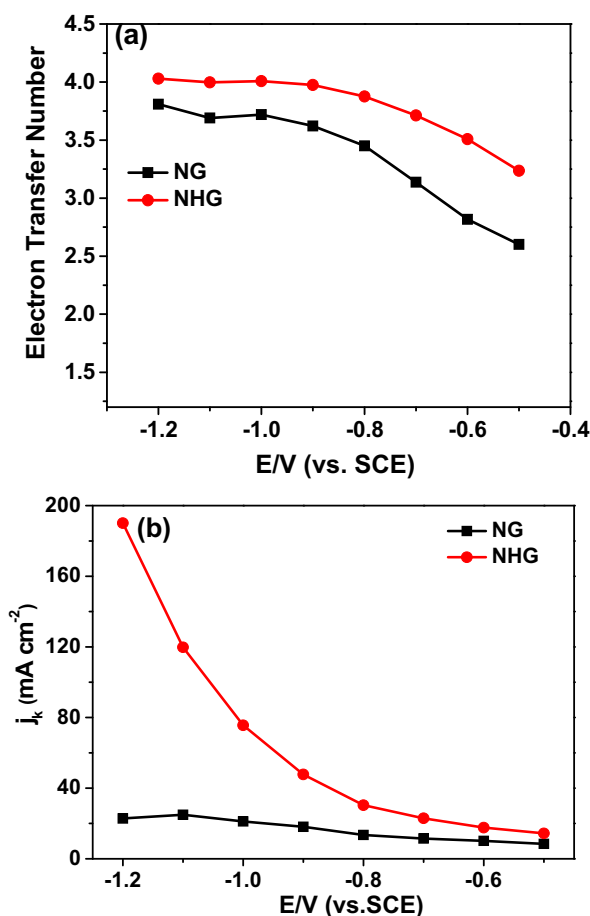
Fig. 11. Dependence of (a) the electron transfer number and (b) the calculated kinetic current density on the potential for the NG and NHG electrodes in the O_2-saturated 0.1 M KOH.
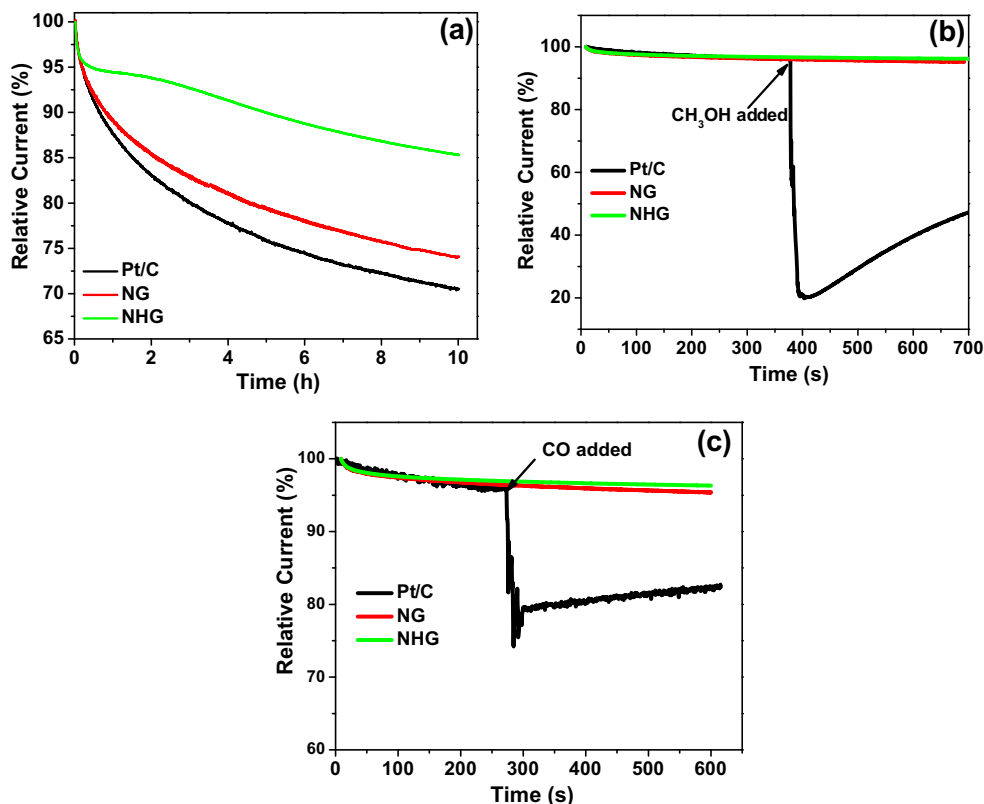
Fig. 12. (a) Durability evaluation of the NG, NHG and Pt/C electrodes for 10 h at −0.35 V and a rotation rate of 1000 rpm. (b) Chronoamperometric responses for the ORR on the NG, NHG and Pt/C electrodes on the addition of 3 M methanol after about 380 s, and (c) chronoamperometric responses for the ORR at the NG, NHG and Pt/C electrodes on the introduction of CO after about 270 s at −0.4 V.

space for ions, faster electrolyte diffusion and movement and so on. We would expect that such NHG could be used as an active material with great potentials for uses in applications in fuel cells and supercapacitors.

References

[1] S. Lee, Y. Cho, H.K. Song, K.T. Lee, J. Cho, Angew. Chem. Int. Ed. 51 (2012) 8748–8752.
[2] D.H. Wang, R. Kou, D. Choi, Z.G. Yang, Z.M. Nie, J. Li, L.V. Saraf, D.H. Hu, J.G. Zhang, G.L. Graff, J. Liu, M.A. Pope, I.A. Aksay, ACS Nano 4 (2010) 1587–1595.
[3] J.D. Wiggins-Camacho, K.J. Stevenson, J. Phys. Chem. C 115 (2011) 20002–20010.
[4] Z. Jiang, Z.-j. Jiang, J. Alloys Compd. 537 (2012) 308–317.
[5] Z. Jiang, B. Pei, A. Manthiram, J. Mater. Chem. A 1 (2013) 7775–7781.
[6] C.G. Liu, Z.N. Yu, D. Neff, A. Zhamu, B.Z. Jang, Nano Lett. 10 (2010) 4863–4868.
[7] Z.-S. Wu, W. Ren, L. Xu, F. Li, H.-M. Cheng, ACS Nano 5 (2011) 5463–5471.
[8] E. Iyyamperumal, S.Y. Wang, L.M. Dai, ACS Nano 6 (2012) 5259–5265.
[9] R.R. Bi, X.L. Wu, F.F. Cao, L.Y. Jiang, Y.G. Guo, L.J. Wan, J. Phys. Chem. C 114 (2010) 2448–2451.
[10] L. Shen, X. Zhang, H. Li, C. Yuan, G. Cao, J. Phys. Chem. Lett. 2 (2011) 3096–3101.
[11] M. Lefevre, E. Proietti, F. Jaouen, J.P. Dodelet, Science 324 (2009) 71–74.
[12] F. Yao, F. Gunes, H.Q. Ta, S.M. Lee, S.J. Chae, K.Y. Sheem, C.S. Cojocaru, S.S. Xie, Y.H. Lee, J. Am. Chem. Soc. 134 (2012) 8646–8654.
[13] X. Wang, H. Guan, S. Chen, H. Li, T. Zhai, D. Tang, Y. Bando, D. Golberg, Chem. Commun. 47 (2011) 12280–12282.
[14] B.G. Choi, M. Yang, W.H. Hong, J.W. Choi, Y.S. Huh, ACS Nano 6 (2012) 4020–4028.
[15] Z. Xu, Z. Li, C.M.B. Holt, X. Tan, H. Wang, B.S. Amirkhiz, T. Stephenson, D. Mitlin, J. Phys. Chem. Lett. 3 (2012) 2928–2933.
[16] Z.-S. Wu, S. Yang, Y. Sun, K. Parvez, X. Feng, K. Müllen, J. Am. Chem. Soc. 134 (2012) 9082–9085.
[17] Y. Sun, C. Li, G. Shi, J. Mater. Chem. 22 (2012) 12810–12816.
[18] H. Wang, Y. Yang, Y. Liang, L.F. Cui, H.S. Casalongue, Y. Li, G. Hong, Y. Cui, H. Dai, Angew. Chem. Int. Ed. 50 (2011) 7364–7368.
[19] A. Caillard, C. Coutanceau, P. Brault, J. Mathias, J.M. Léger, J. Power Sources 162 (2006) 66–73.
[20] Z. Jiang, X. Yu, Z.-j. Jiang, Y. Meng, Y. Shi, J. Mater. Chem. 19 (2009) 6720–6726.
[21] J. Liu, Z. Jiang, Z.-j. Jiang, Y. Meng, J. Mater. Chem. 21 (2011) 5565–5568.
[22] S. Shanmugam, T. Osaka, Chem. Commun. 47 (2011) 4463–4465.
[23] G. Wang, J. Yang, J. Park, X. Gou, B. Wang, H. Liu, J. Yao, J. Phys. Chem. C 112 (2008) 8192–8195.
[24] D.W. Boukhvalov, M.I. Katsnelson, J. Phys. Chem. C 113 (2009) 14176–14178.
[25] C.N.R. Rao, H.S.S. Ramakrishna-Matte, K.S. Subrahmanyam, Acc. Chem. Res. 46 (2013) 149–159.
[26] Y. Jiang, T. Yuan, W. Sun, M. Yan, ACS Appl. Mater. Interfaces 4 (2012) 6216–6220.
[27] X.C. Chen, W. Wei, W. Lv, F.Y. Su, Y.B. He, B. Li, F. Kang, Q.H. Yang, Chem. Commun. 48 (2012) 5904–5906.
[28] E. Yoo, J. Kim, E. Hosono, H.-S. Zhou, T. Kudo, I. Honma, Nano Lett. 8 (2008) 2277–2282.
[29] X. Zhao, L. Zhang, S. Murali, M.D. Stoller, Q. Zhang, Y. Zhu, R.S. Ruoff, ACS Nano 6 (2012) 5404–5412.
[30] R. Mukherjee, A.V. Thomas, A. Krishnamurthy, N. Koratkar, ACS Nano 6 (2012) 7867–7878.
[31] C. Wang, D. Li, C.O. Too, G.G. Wallace, Chem. Mater. 21 (2009) 2604–2606.
[32] T. Bhardwaj, A. Antic, B. Pavan, V. Barone, B.D. Fahlman, J. Am. Chem. Soc. 132 (2010) 12556–12558.
[33] G. Wang, B. Wang, X. Wang, J. Park, S. Dou, H. Ahn, K. Kim, J. Mater. Chem. 19 (2009) 8378–8384.
[34] T. Maiyalagan, X. Dong, P. Chen, X. Wang, J. Mater. Chem. 22 (2012) 5286–5290.
[35] X. Cao, Y. Shi, W. Shi, G. Lu, X. Huang, Q. Yan, Q. Zhang, H. Zhang, Small 7 (2011) 3163–3168.
[36] B. You, L. Wang, L. Yao, J. Yang, Chem. Commun. 49 (2013) 5016–5018.

[37] X.C. Dong, H. Xu, X.W. Wang, Y.X. Huang, M.B. Chan-Park, H. Zhang, L.H. Wang, W. Huang, P. Chen, ACS Nano 6 (2012) 3206–3213.
[38] Z. Lin, M.K. Song, Y. Ding, Y. Liu, M. Liu, C.P. Wong, Phys. Chem. Phys. 14 (2012) 3381–3387.
[39] L. Lai, J.R. Potts, D. Zhan, L. Wang, C.K. Poh, C. Tang, H. Gong, Z. Shen, J. Lin, R.S. Ruoff, Energy Environ. Sci. 5 (2012) 7936–7942.
[40] S.-Y. Yang, K.-H. Chang, H.-W. Tien, Y.-F. Lee, S.-M. Li, Y.-S. Wang, J.-Y. Wang, C.-C.M. Ma, C.-C. Hu, J. Mater. Chem. 21 (2011) 2374–2380.
[41] B.G. Choi, S.-J. Chang, Y.B. Lee, J.S. Bae, H.J. Kim, Y.S. Huh, Nanoscale 4 (2012) 5924–5930.
[42] F. Du, Y. Liu, A. Perez, M. Supp, T.S. Ramakrishnan, L. Dai, L. Jiang, J. Am. Chem. Soc. 132 (2010) 15839–15841.
[43] Y. Ma, L. Sun, W. Huang, L. Zhang, J. Zhao, Q. Fan, W. Huang, J. Phys. Chem. C 115 (2011) 24592–24597.
[44] K. Parvez, S. Yang, Y. Hernandez, A. Winter, A. Turchanin, X. Feng, K. Müllen, ACS Nano 6 (2012) 9541–9550.
[45] S. Wang, L. Zhang, Z. Xia, A. Roy, D.W. Chang, J.B. Baek, L. Dai, Angew. Chem. Int. Ed. 51 (2012) 4209–4212.
[46] Z. Yang, Z. Yao, G. Li, G. Fang, H. Nie, Z. Liu, X. Zhou, X.a. Chen, S. Huang, ACS Nano 6 (2011) 205–211.
[47] L. Qie, W.M. Chen, Z.H. Wang, Q.G. Shao, X. Li, L.X. Yuan, X.L. Hu, W.X. Zhang, Y.H. Huang, Adv. Mater. 24 (2012) 2047–2050.
[48] H. Wang, C. Zhang, Z. Liu, L. Wang, P. Han, H. Xu, K. Zhang, S. Dong, J. Yao, G. Cui, J. Mater. Chem. 21 (2011) 5430–5434.
[49] H.M. Jeong, J.W. Lee, W.H. Shin, Y.J. Choi, H.J. Shin, J.K. Kang, J.W. Choi, Nano Lett. 11 (2011) 2472–2477.
[50] Y. Qiu, X. Zhang, S. Yang, Phys. Chem. Chem. Phys. 13 (2011) 12554–12558.
[51] L. Yang, S. Jiang, Y. Zhao, L. Zhu, S. Chen, X. Wang, Q. Wu, J. Ma, Y. Ma, Z. Hu, Angew. Chem. Int. Ed. 50 (2011) 7132–7135.
[52] S.L. Candelaria, B.B. Garcia, D. Liu, G. Cao, J. Mater. Chem. 22 (2012) 9884–9889.
[53] X.Q. Yang, D.C. Wu, X.M. Chen, R.W. Fu, J. Phys. Chem. C 114 (2010) 8581–8586.
[54] W.S. Hummers, R.E. Offeman, J. Am. Chem. Soc. 80 (1958) 1339–1339.
[55] Y.W. Zhu, S. Murali, M.D. Stoller, K.J. Ganesh, W.W. Cai, P.J. Ferreira, A. Pirkle, R.M. Wallace, K.A. Cychosz, M. Thommes, D. Su, E.A. Stach, R.S. Ruoff, Science 332 (2011) 1537–1541.
[56] V. Barranco, M.A. Lillo-Rodenas, A. Linares-Solano, A. Oya, F. Pico, J. Ibañez, F. Agullo-Rueda, J.M. Amarilla, J.M. Rojo, J. Phys. Chem. C 114 (2010) 10302–10307.
[57] L.L. Zhang, X. Zhao, M.D. Stoller, Y. Zhu, H. Ji, S. Murali, Y. Wu, S. Perales, B. Clevenger, R.S. Ruoff, Nano Lett. 12 (2012) 1806–1812.
[58] I.-Y. Jeon, H.-J. Choi, S.-M. Jung, J.-M. Seo, M.-J. Kim, L. Dai, J.-B. Baek, J. Am. Chem. Soc. 135 (2013) 1386–1393.
[59] I.-Y. Jeon, H.-J. Choi, M. Choi, J.-M. Seo, S.-M. Jung, M.-J. Kim, S. Zhang, L. Zhang, Z. Xia, L. Dai, N. Park, J.-B. Baek, Sci. Rep. 3 (2013) 1810–1816.
[60] Y. Zhang, K. Fugane, T. Mori, L. Niu, J. Ye, J. Mater. Chem. 22 (2012) 6575–6580.
[61] M.-C. Hsiao, S.-H. Liao, M.-Y. Yen, P.-I. Liu, N.-W. Pu, C.-A. Wang, C.-C.M. Ma, ACS Appl. Mater. Interfaces 2 (2010) 3092–3099.
[62] M.A. Piment, G. Dresselhaus, M.S. Dresselhaus, L.G. Cancado, A. Jorio, R. Saito, Phys. Chem. Chem. Phys. 9 (2007) 1276–1291.
[63] X. Zhang, Z. Sui, B. Xu, S. Yue, Y. Luo, W. Zhan, B. Liu, J. Mater. Chem. 21 (2011) 6494–6497.
[64] Z. Jiang, X. Zhao, Y. Fu, A. Manthiram, J. Mater. Chem. 22 (2012) 24862–24869.
[65] W.-Y. Tsai, R. Lin, S. Murali, L. Zhang, J.K. McDonough, R.S. Ruoff, P.-L. Taberna, Y. Gogotsi, P. Simon, Nano Energy 2 (2013) 403–411.
[66] E. Frackowiak, J. Braz. Chem. Soc. 17 (2006) 1074–1082.
[67] L. Qu, Y. Liu, J.-B. Baek, L. Dai, ACS Nano 4 (2010) 1321–1326.
[68] S. Wang, D. Yu, L. Dai, D.W. Chang, J.-B. Baek, ACS Nano 5 (2011) 6202–6209.
[69] L. Zhang, Z. Xia, J. Phys. Chem. C 115 (2011) 11170–11176.
[70] H. Uchida, K. Izumi, M. Watanabe, J. Phys. Chem. B 110 (2006) 21924–21930.
[71] Y. Yu, H.L. Xin, R. Hovden, D. Wang, E.D. Rus, J.A. Mundy, D.A. Muller, H.D. Abruña, Nano Lett. 12 (2012) 4417–4423.
[72] J.C. Davies, G. Tsotridis, J. Phys. Chem. C 112 (2008) 3392–3397.
[73] Q. Ge, S. Desai, M. Neurock, K. Kourtakis, J. Phys. Chem. B 105 (2001) 9533–9536.